

Numerical Investigation of Shock/Film-Cooling Interaction

K. Ozawa*, S. Loosen**, M. Albers**, P. S. Meysonnat**, M. Meinke**,
W. Schröder** and S. Obayashi*

Corresponding author: ozawa@edge.ifs.tohoku.ac.jp

* Institute of Fluid Science, Tohoku University, Japan.

** Institute of Aerodynamics, RWTH Aachen University, Germany.

Abstract: In this numerical study, a film-cooling flow with shock-wave interaction is analyzed using large-eddy simulation (LES). A laminar cooling film at an injection Mach number of $Ma_i = 1.8$ is injected through a slot into a fully turbulent boundary layer at a freestream Mach number of $Ma_\infty = 2.44$. An oblique shock, generated by a flow deflection of $\beta = 5^\circ$ or 8° , impinges upon the cooling film within the potential-core region. At a deflection angle of $\beta = 5^\circ$, the cooling effectiveness downstream the shock impingement is decreased by 4.6% compared to the undisturbed flow configuration. A flow deflection of $\beta = 8^\circ$ leads to a decrease in cooling effectiveness of 13.4%. The separation bubble at the shock impingement position causes a strong negative peak of the Reynolds shear stress near the wall. With increasing shock strength, the separation bubble significantly grows in size. The separation length of the strong shock configuration is increased by a factor of 4.6 compared to the weaker shock configuration.

Keywords: Slot-Film Cooling, Shock-Cooling Film Interaction, Supersonic Flow, LES.

1 Introduction

In a supersonic combustion ramjet, also known as a scramjet, shock waves occur in the isolator and combustion chamber. To protect the engine's interior surfaces from intense aerodynamic heating, film cooling is a promising cooling concept [1]. The cooling effectiveness, however, is decreased by oblique shocks interacting with the film-cooling flow. Fig. 1 sketches the basic structures of the flow field of a tangential film-cooling configuration with shock wave interaction [2, 3]. The flow field can be divided into three regions [1, 4]. The first region is the potential-core region just downstream of the slot, in which the maximum velocity in the cooling film is unaffected by the outer boundary layer. Further downstream, in the wall-jet region, the slot boundary layer merges with the mixing layer which forms between the film cooling flow and the outer boundary layer. In the third region, the boundary-layer region, the flow relaxes to an undisturbed turbulent boundary layer. To examine the decrease of the cooling effectiveness caused by shock wave interaction Alzener & Zakkay [5] experimentally investigated the interaction at a freestream Mach number of $Ma_\infty = 6$ with and without injection to measure the cooling effectiveness. An experiment performed by Kanda et al. [6] and Kanda & Ono [7] at sonic injection with shock wave interaction at a freestream Mach number of $Ma_\infty = 2.35$, showed that the cooling effectiveness is determined by the wall-recovery temperature and is not significantly affected by the shock interaction. A numerical analysis using large-eddy simulation (LES) was performed by Konopka et al. [2, 3], who investigated injection Mach numbers of $Ma_i = 1.2$ & 1.8 into supersonic turbulent boundary layers. The authors concludes that the lower injection Mach number significantly decreases the cooling effectiveness compared to the higher injection Mach number. Marquardt et al. [8, 9] performed high-speed particle-image velocimetry (PIV) measurements to investigate the details of the flow field. They concluded that the shock leads to a highly disturbed flow with a large separation bubble at a low injection Mach number of $Ma_i = 1.2$. Furthermore, a shock impingement in the wall-jet

region leads to a larger separation bubble and stronger turbulent mixing than a shock impingement in the potential-core region.

The potential-core region, which originates at the slot, is encompassed by the slot boundary layer and the mixing layer, i.e., the shear layer emanating from the nozzle lip. When shock waves interact with the cooling film within the potential-core region, the shock waves change the fundamental structure of the flow field in the vicinity of the surfaces that require cooling, which in turn can reduce the cooling effectiveness. Therefore, this study investigates film-cooling flows interacting with shock waves with different shock angles by numerical simulation and compares the data to experiments by Marquardt *et al.* [8]. In this investigation a cooling film at an injection Mach number of $Ma_i = 1.8$ is injected into a supersonic turbulent boundary layer at a freestream Mach number of $Ma_\infty = 2.44$. First, the numerical method, boundary conditions and the computational mesh will be described. Then, the flow configurations will be defined and the results will be discussed. The results section includes a comparison of the turbulence statistics of the inflow boundary layer upstream of the slot to the direct numerical simulation (DNS) data of Pirozzoli & Bernardini [10, 11, 12]. Finally, the film-cooling flow with shock wave interaction is analyzed in terms of cooling effectiveness, instantaneous flow fields and turbulence statics.

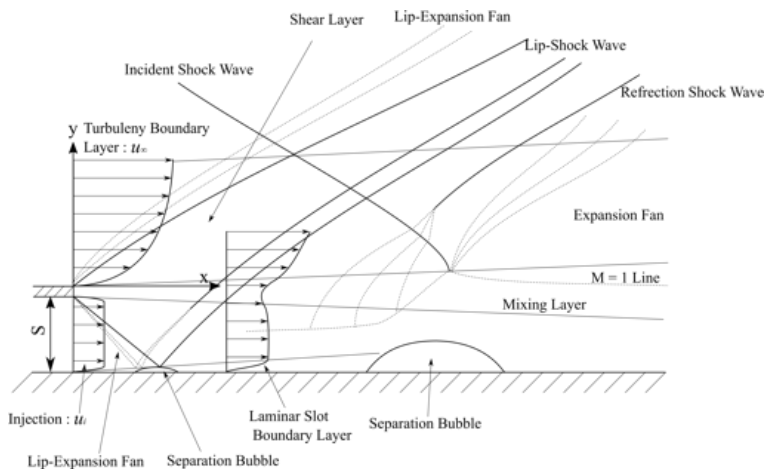


Figure 1: Flow schematic with velocity profiles indicating the shock interaction.

2 Numerical Method

Previous investigations of shock/film-cooling interaction often employed Reynolds-Averaged Navier-Stokes (RANS) simulations, e.g. using the $k-\epsilon$ turbulence model [13]. Most of these models, however, tend to deliver inaccurate results for separating flows with strong temperature or density gradients, whereas it was shown by Konopka *et al* [2, 3] that high resolution large-eddy (LES) simulations can correctly predict the averaged flow statistics. Therefore, in this study the compressible unsteady three-dimensional Navier-Stokes equations are discretized using a high-resolution LES approach at second-order accuracy. The inviscid fluxes are discretized by the Advection Upstream Splitting Method (AUSM) by Liou and Steffen [14], where the cell-surface values of the flow quantities are reconstructed by a MUSCL type scheme for stretched meshes. The viscous fluxes are discretized using a modified cell-vertex scheme and the temporal discretization is performed via a five-stage Runge-Kutta scheme. The dissipation at the smallest, unresolved, scales is modeled implicitly using the monotonically integrated LES (MILES) approach [15]. That is, the numerical dissipation of the second-order accurate discretization method takes the role of the dissipation of the unresolved scales. More details of the flow solver used in this study are given by Roidl *et al.* [16].

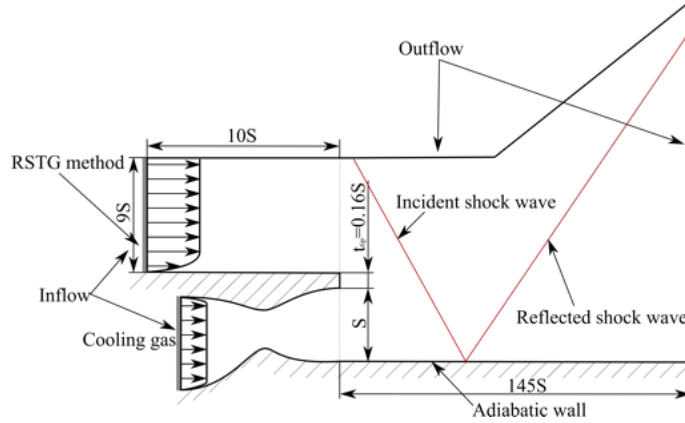


Figure 2: Sketch of the physical domain including the incoming boundary layer, the nozzle and interaction parts.

3 Flow Setup

The physical domain of the flow setup considered in this investigation is depicted in Fig. 2, with the flow regions of the incoming turbulent boundary layer, the Laval nozzle of the cooling-gas flow, and the interaction region between the film-cooling flow, the turbulent shear layer, and the shock. The total length of the flow domain is $L_x = 145S$, where $S = 1.0$ is the nozzle height at the outlet of the cooling-gas. The lip thickness is $t_{lip} = 0.16S$. The spanwise domain width is chosen to be $z = 4S$, which is large enough to resolve the large scale structures developing in the shock boundary layer interaction region. Adiabatic no-slip boundary conditions are used at all solid walls of the flow domain and fully periodic boundary conditions are imposed in the spanwise direction. The incoming flow of the boundary layer is generated by the reformulated synthetic turbulence generation (RSTG) method [16], which ensures a transition to a fully-developed turbulent boundary layer within 4 – 6 boundary layer thicknesses. At the inflow of the cooling-gas nozzle a subsonic laminar velocity distribution is defined with thin laminar boundary layers near the wall. The shock wave in the film-cooling domain is prescribed using the Rankine-Hugoniot relations such that on the upper boundary the flow variables satisfy the required shock angle and shock strength. Downstream of the shock wave the computational domain is extended in the wall-normal direction to ensure the reflected shock wave to exit the computational domain via the outflow boundary.

The physical domain is discretized using a block-structured curvilinear mesh, adequately refined in the regions of large flow gradients and turbulent flow. The maximum wall resolution in the region of the incoming turbulent boundary layer is $\Delta x^+ = 7.5$, $\Delta y^+ = 1.0$, $\Delta z^+ = 7.6$ in inner units in the streamwise, wall-normal, and spanwise direction, respectively. Around the lip and the shock impingement position the mesh resolution is increased, as shown in Fig. 3, to accurately capture the shock flow gradients. An equidistant spacing is chosen in the spanwise direction. A grid study for this film-cooling configuration was performed by Konopka et al. [2, 3], where the current resolution is found to be adequate. In total, the grid, depicted in Fig. 3, consists of $n \approx 286 \cdot 10^6$ grid points for cases I and II, and $n = 383 \cdot 10^6$ grids points for case III.

The injection condition and the freestream flow configuration are chosen as in the experiments by Marquardt *et al* [8, 9], who used a trisonic wind tunnel to accelerate air from ambient conditions to a freestream Mach number of $Ma_\infty = 2.45$. The parameters of the three supersonic cooling configurations are summarized in Tab. 3. The freestream Reynolds number $Re_\infty = u_\infty S / \nu_\infty$, based on the slot height S , the freestream velocity u_∞ , and the freestream kinematic viscosity ν_∞ , is $Re_\infty = 42000$. The Reynolds number of the slot flow $Re_i = u_i S / \nu_i$ based on the centerline velocity and kinematic viscosity of the slot is $Re_i = 29379$. A constant subsonic velocity profile is prescribed at the inflow of the Laval nozzle, such that supersonic flow at a Mach number of $Ma_i = 1.8$ is achieved at the slot outlet. The blowing rate M is computed by the integrated mass flow through the slot divided by the slot height S . Case I is the reference case without an outer shock wave impinging upon the cooling film. The shocks in cases II and III are generated by a flow deflection of $\beta = 5^\circ$ (case II) and 8° (case III) and impinge at 17 slot heights downstream of the slot. Case

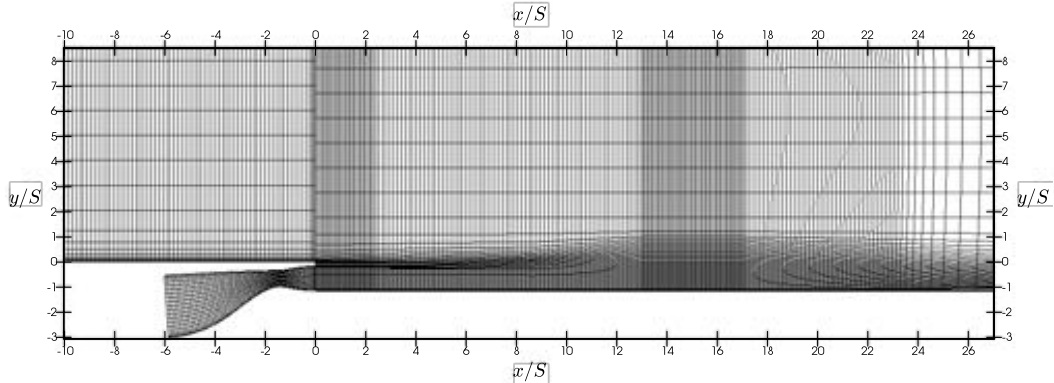


Figure 3: Two-dimensional slice of the three-dimensional numerical mesh for case I and II; only every tenth grid point is shown for clarity.

I is a configuration without shock and for which a validation is performed in section 4.1 by comparing the results with the DNS data of Pirozzoli & Bernardini [10, 11, 12].

Case	Ma_∞	x_{imp}/S	β [deg]	σ [deg]	Ma_i	$T_{ti}/T_{t\infty}$	$M = \rho_i u_i / (\rho_\infty u_\infty)$
I	2.44	-	-	-	1.8	0.76	0.636
II	2.44	17	5	28.07	1.8	0.76	0.636
III	2.44	17	8	30.68	1.8	0.76	0.636

Table 1: Flow parameters of the three setups.

4 Results

The discussion of the results is divided into four parts. First, a validation of the turbulent inflow boundary layer and the laminar slot film flow is presented. Second, the supersonic film-cooling configuration case I, i.e., the configuration without shock is examined. Then, the flow characteristics of the interaction of a supersonic cooling film with shock waves, i.e., cases II and III, are presented, followed by an analysis of the instantaneous flow fields. Subsequently, the impact of the shocks and their impingement location on the cooling effectiveness, the mean flow field, and the turbulence statistics is investigated.

4.1 Validation of the Incoming Turbulent Boundary Layer

The reformulated synthetic turbulent generation (RSTG) method [16] is used to generate a turbulent boundary layer upstream of the injection slot. The freestream Reynolds number based on the momentum thickness of the boundary layer is $Re_\theta = 6537$ at $x/S = -2$, i.e., two injection gap heights upstream of the lip, and the freestream Mach number is $Ma_\infty = 2.44$. Fig. 4(a) shows the streamwise velocity profile non-dimensionalized by the freestream velocity u_∞ and Fig. 4(b) shows the same profile scaled by the van Driest transformation [17]. For validation purposes, the results of the DNS from Pirozzoli & Bernardini [10, 11, 12] at $Ma = 2.0$ and $Re_\theta = 6044$ are also shown in the figures and in addition the law of the wall is given in Fig. 4(b). The logarithmic region compares well with the law of the wall, i.e., $u^+ = 1/0.41 \cdot \ln y^+ + 5.2$, and the results of Pirozzoli & Bernardini [10, 11, 12]. The small differences in the wake region are due to the higher freestream Mach number and Re_θ compared to the reported DNS results. The distribution of the Reynolds stress components including u_{rms}/u_τ , v_{rms}/u_τ , w_{rms}/u_τ and $\overline{u'v'}/u_\tau^2$ are shown in Fig. 4(c). The results are in good qualitative and quantitative agreement with the results of the DNS [10, 11, 12].

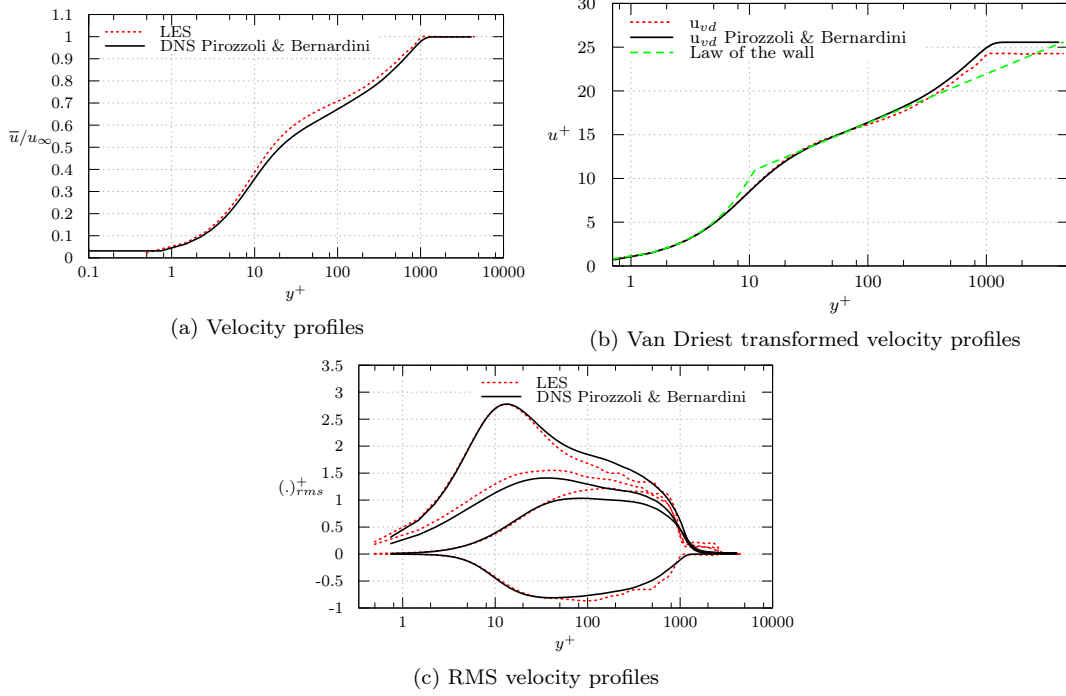


Figure 4: Velocity profiles, van Driest transformed velocity profiles in wall units and RMS velocity profiles vs. y/S , u_{rms}/u_τ , v_{rms}/u_τ , w_{rms}/u_τ and $u'v'/u_\tau^2$ compared to the data of Pirozzoli & Bernardini [10, 11, 12].

4.2 Validation of the Slot Injection Flow

In this study the same Laval nozzle geometry for the slot injection is used as in the experimental investigation of Marquardt et al. [8, 9]. The injection Mach number obtained at the exit of the Laval nozzle is $Ma_i = 1.8$. The streamwise Mach number and static pressure distribution in the center of the nozzle are shown in Fig. 6(a) and (b) along with the theoretical isotropic values. The mass flow Q_{LES} through the nozzle is almost identical, i.e., only 0.4% smaller, compared to the experimental setup [8, 9]. A qualitative and quantitative satisfying agreement can be observed with the theoretical data. Fig. 6 shows the Mach number and the static temperature contours in the nozzle. It is visible that the Mach number and the static temperature at the end of the nozzle match the target values for the cooling film injection.

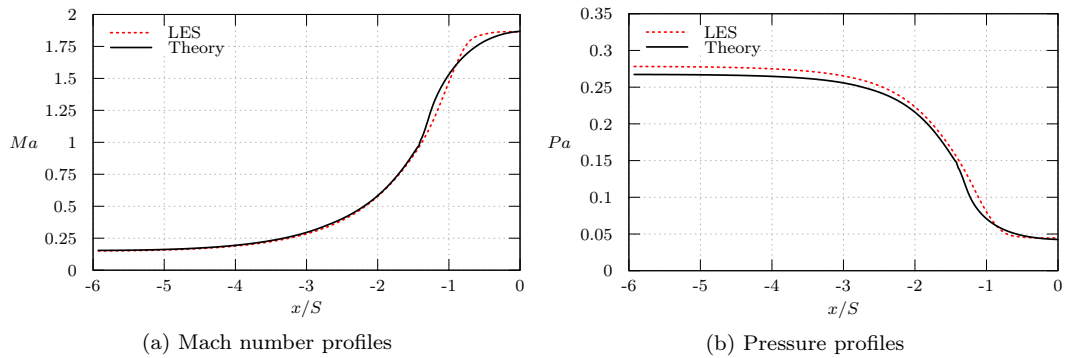


Figure 5: Streamwise Mach number and pressure distribution in the center between the top and bottom wall vs. x/S .

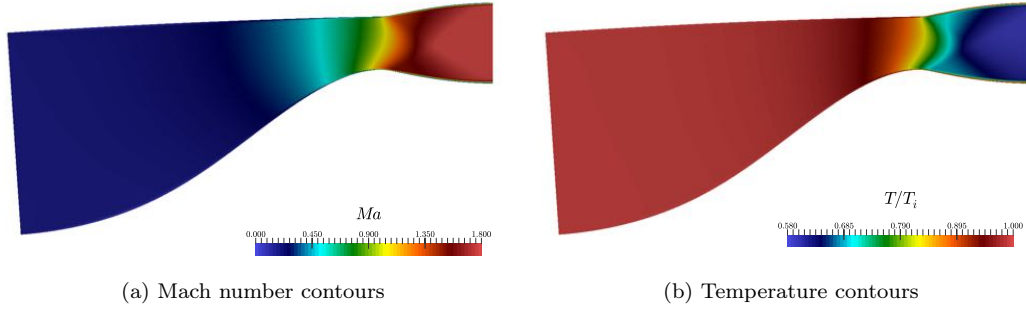


Figure 6: Mach number and temperature contours.

4.3 Film cooling without impinging shock (case I)

The flow setup without shock serves as a baseline case to analyze the effect of the shock waves in cases II and III and is discussed first. The Mach number contours and streamwise velocity profiles of case I are shown in Fig. 7 and 8(a). In Fig. 8(a) the potential-core region starting at $x/S = 0$ is visible, where the velocity is constant in wall normal direction in the area downstream of the slot between $-1.16 \leq y/S \leq -0.16$. The region with constant velocity becomes smaller in downstream direction and vanishes in the expanding mixing layer emanating from the lip. Fig. 8(b) shows the Reynolds stress component $\overline{u'v'}/u_\infty^2$, which is responsible for the momentum exchange in wall normal direction. Since the ejected flow from the Laval nozzle is laminar, the shear stress is zero in the potential-core region. The distribution of the Reynolds stresses u_{rms}^+ and v_{rms}^+ are shown in Fig. 8(c) and (d). All these distributions show that no fully turbulent boundary layer is obtained until $x/S = 22$. In Fig. 8(b,c,d) a peak in the velocity fluctuations near the bottom wall is generated by the unsteady shock wave, which emanates from the lip. This generates a streamwise component u_{rms}^+ which is larger than the wall normal component v_{rms}^+ . All Reynolds stress tensor components are increasing in magnitude in downstream direction above the wall and merge with the distributions of the above free shear layer.

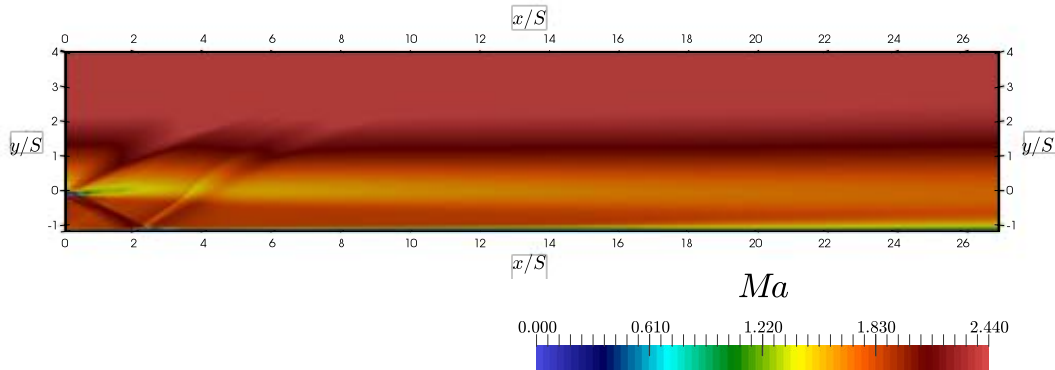


Figure 7: Mach number contour (Case I).

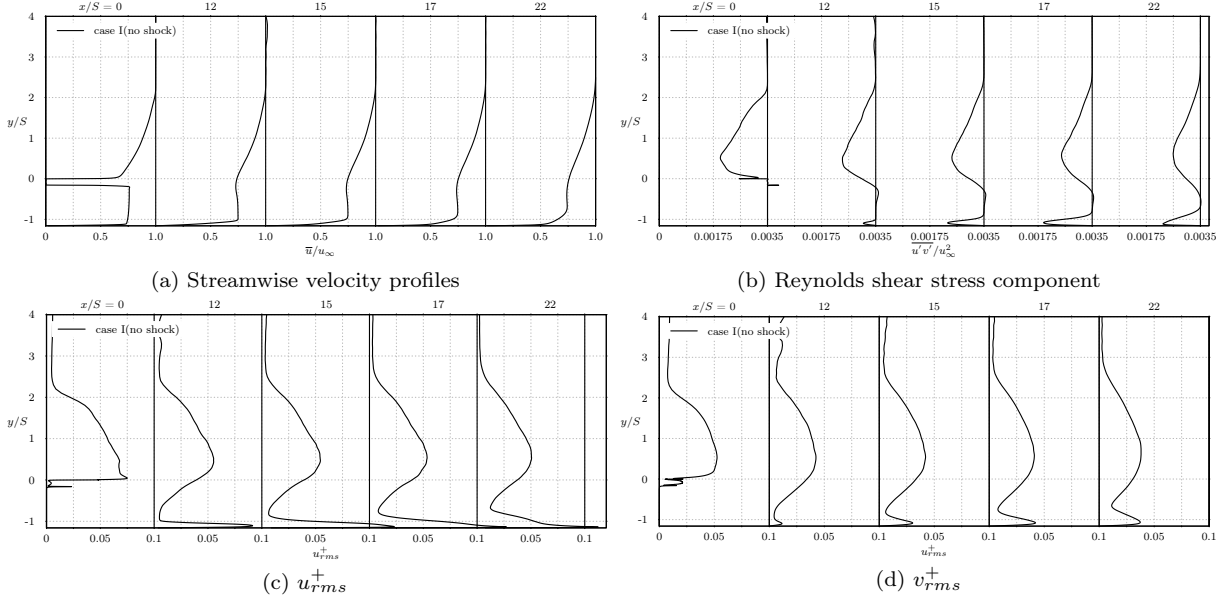


Figure 8: Streamwise velocity profiles and distribution of Reynolds stress components for case I

4.4 Analysis of the Shock/Film-Cooling Interaction

In the following, cases II and III are analyzed to understand the effect of the shock on the cooling effectiveness and the turbulence statistics.

4.4.1 Mean Flow Field

Fig. 9 shows the Mach number contours exhibiting the cooling-film shock interaction of cases II and III. Downstream of the shock impingement position, i.e., $x/S = 15$, the low Mach number region near the wall is caused by a separation bubble. A larger separation bubble in the configuration with a flow deflection of 8° is caused by the larger strength of the incident shock wave.

The skin-friction coefficient distribution downstream of the lip is shown in Fig. 10(a) for all three cases. The skin friction rises quickly at $x/S = 2$, where the shock wave emanating from the lip hits the lower wall. At the impingement position, a separation bubble with a length of $L_{sep}/S = 1.09$ exists in all three cases. The results of Konopka et al. show a length of $L_{sep}/S = 0.16$, which can be explained by the different slot velocity profile used in this paper. At the main shock-impingement position at $x/S = 15$, a separation bubble with a length of $L_{sep}/S = 0.36$ exists for case II. The stronger shock in case III, which results from the larger deflection angle $\beta = 8^\circ$, leads to a significant larger separation with a length of $L_{sep}/S = 1.64$. In addition, the minimum skin-friction coefficient is slightly smaller compared to case II. Downstream of the shock impingement the skin friction and the pressure fluctuations, Fig. 10(b), rise abruptly, indicating a transition to a turbulent boundary layer. A comparison of the present results to those by Konopka et al. shows the following differences. In the present results for case I, the skin friction rises gradually after $x/S = 13$ and the separation bubble in case II starts at $x_S/S = 14.6$ and ends at $x_{Smax}/S = 14.9$. The separation bubble of Konopka et al. starts at $x_S/S = 9.8$ and ends at $x_{Smax}/S = 15.6$. These differences can be explained by the lower Reynolds number used in the setup of Konopka et al.

4.4.2 Instantaneous Flow Field

The Q criterion visualizing the vortical structures of case III with shock interaction is shown in Fig. 11, where the coloring represents the Mach number. No vortical structures are visible in the injected flow, since it is laminar. After the impingement of the lip shock weak vortical structures are visible above the wall. Above the lip at $y/S \geq 0$ the vortical structures stemming from the turbulent boundary layer are visible. The

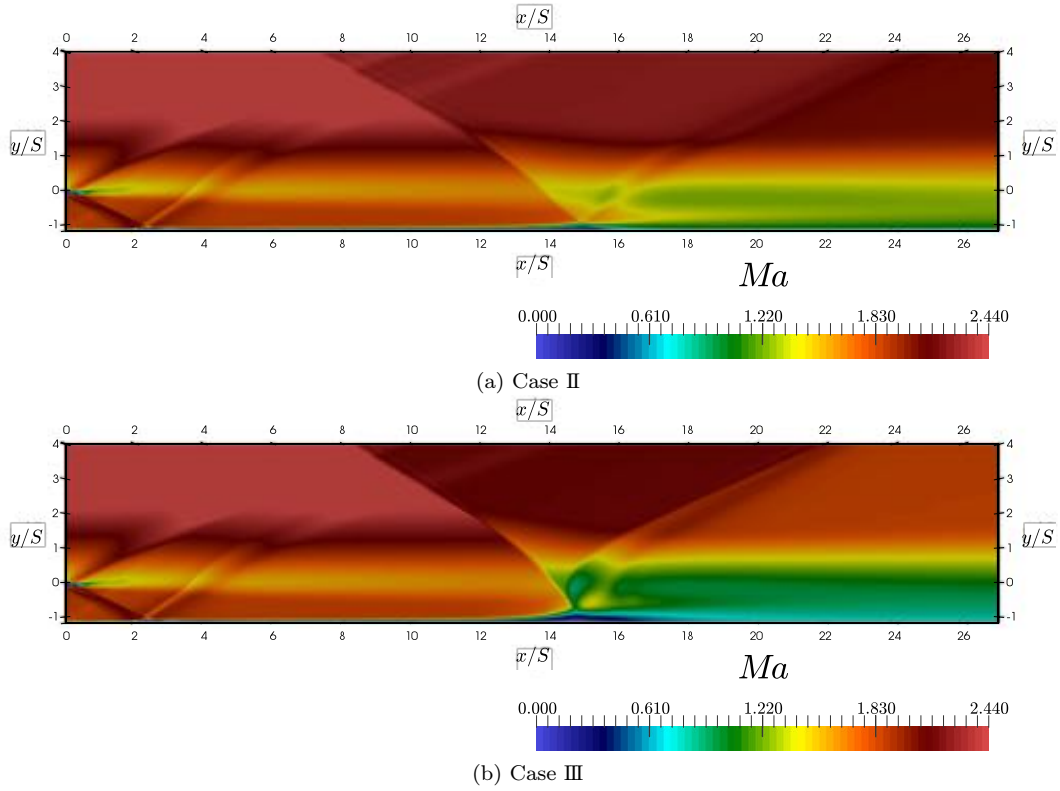


Figure 9: Mach number contour of cases II and III.
Fig. 10(b).

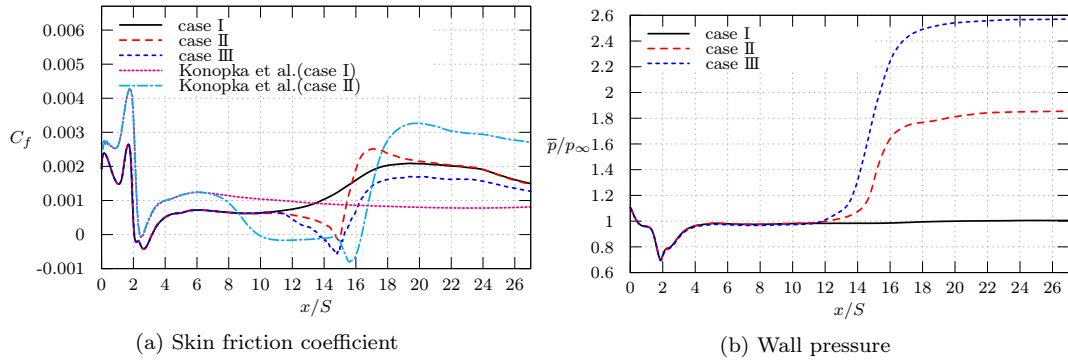


Figure 10: Skin friction coefficient (a) and wall pressure distribution (b) plotted vs. the streamwise distance from the slot

free turbulent shear layer is then penetrated by the shock wave, which generates turbulent scales up- and downstream of the shock impingement position.

An instantaneous numerical schlieren image is shown in Fig. 12 to visualize the flow field of case III in a cut plane. The laminar slot flow is clearly visible until it mixes with the mixing layer due to the shock wave interaction. The incident shock wave is reflected at $x/S = 14.5$ and a high turbulence level is apparent near the wall downstream of the impingement point of the shock.

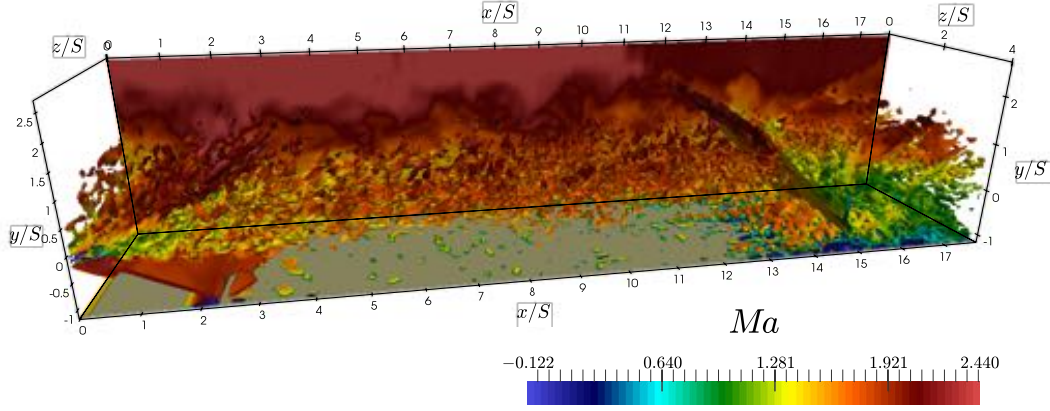


Figure 11: Q criterion with mapped-on Mach number contours (case III).

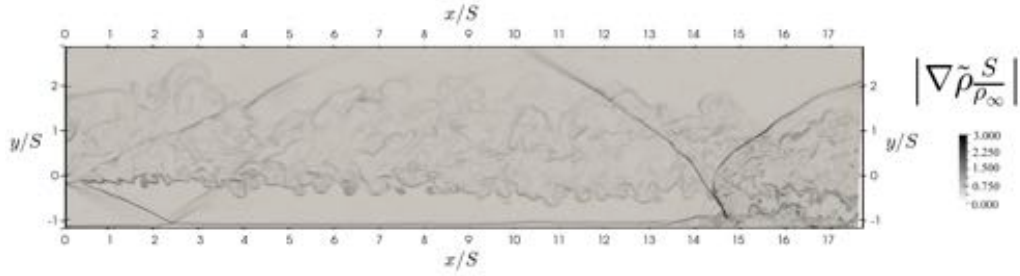


Figure 12: Instantaneous numerical Schlieren image (case III).

4.4.3 Cooling Effectiveness

To obtain the cooling effectiveness the reference recovery temperature is computed by

$$T_r = T_e \left(1 + r \frac{\gamma - 1}{2} Ma_e^2 \right) \quad (1)$$

where T_e and Ma_e are the temperature and Mach number at the boundary layer edge, and r is the recovery factor. In the laminar slot the recovery factor is $r = \sqrt{Pr}$ and for the turbulent freestream boundary layer $r = \sqrt[3]{Pr}$ is used. The spanwise and time averaged cooling effectiveness in the current analysis is defined by

$$\eta = \frac{\tilde{T}_{aw} - T_{r\infty}}{T_{ri} - T_{r\infty}} \quad , \quad (2)$$

where \tilde{T}_{aw} is the Favre-averaged adiabatic wall temperature, $T_{r\infty}$ is the freestream recovery temperature, and $T_{i\infty}$ is the recovery temperature of the cooling flow as computed by Eq. 1. Fig. 13(a) shows the wall temperature as a function of the streamwise direction for all investigated cases and in Fig. 13(b) the corresponding cooling effectiveness is depicted. The cooling effectiveness is slightly above unity around $x/S = 1.8$ since the expansion fan and shock wave emanating from the lower tip of the lip impinge upon the laminar slot boundary layer. At $x_S/S = 14.6$ the cooling effectiveness starts to be reduced at the separation point of the laminar slot boundary layer for case II and at $x_S/S = 13.6$ for case III. The cooling effectiveness decreases further after the transition to the turbulent flow downstream of the separation bubble due to the

merging of the boundary layer with the mixing layer. For case III the cooling effectiveness decays faster compared for case II.

The wall-temperature in Fig. 13(b) shows a similar, but inverse behavior. That is, when the cooling effectiveness decreases the wall-temperature increases. Thus at $x_S/S = 14.6$ for case II and at $x_S/S = 13.6$ for case III, where the shock impinges, the wall-temperature increases.

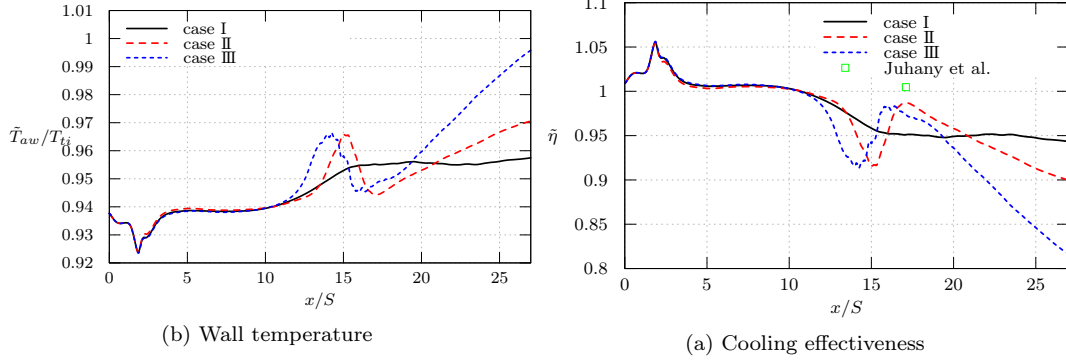


Figure 13: Wall temperature (a) and cooling effectiveness (b) plotted vs. the streamwise distance from the slot for all cases.

4.4.4 Mean Temperature Field

The dimensionless total fluid temperature is defined by

$$\Theta = \frac{\tilde{T}_t - T_{t\infty}}{T_{ti} - T_{t\infty}}, \quad (3)$$

where \tilde{T}_t is the total temperature at the wall used as a reference temperature, $T_{t\infty}$ is the freestream total temperature and T_{ti} is the injection total temperature. That is, the quantity Θ reaches the value of 1 for the cooling flow and 0 for the freestream flow. This definition is used to evaluate the impact of the shock wave on the slot boundary layer and on the mixing layer near the wall. Near the wall the mixing layer is merging towards the slot boundary layer. Due to the shock wave interaction which causes a strong mixing near the wall, the dimensionless total temperature of cases II and III are lower than that of case I downstream of the impingement. For the stronger shock interaction (case III), the dimensionless total temperature is slightly above that of case II around the shock impingement position. Upstream, i.e., at $x/S = 17$, the area of dimensionless fluid temperatures where Θ is greater than 1 for cases II and III near the wall is expanded compared to case I. The area of dimensionless fluid temperature at case III is more affected than that of case II.

Next, the impact of the shock wave on the turbulent kinetic energy (TKE), defined as:

$$k = \frac{1}{2} \left(\overline{u'^2} + \overline{v'^2} + \overline{w'^2} \right), \quad (4)$$

is analyzed in the near-wall region. In Fig. 15 high values of the TKE appear near the wall, which are initiated by the fluctuating shock emanating from the lip and which are growing in the wall boundary layer. The peak in the TKE distribution outside the wall boundary layer is generated by the interaction of the impinging and reflected stronger shock. The absolute values of the TKE at $x/S = 15$ for case III is larger than that of case II, since the stronger shock wave causes a larger separated flow area near the wall. At $x/S = 12$ the value for case III is slightly larger than that of cases I and II because of the different starting point of the separation bubble. The location of the peak is shifted off the wall further downstream.

Fig. 16 shows the Reynolds shear stress profiles of the simulations compared to experimental data from Marquardt et al. [8, 9]. Around the streamwise location of $x/S = 17$, i.e., the location of the shock impingement, a negative peak is shown at $y/S = -1.06$ for case II and -0.92 for case III, where the absolute value for

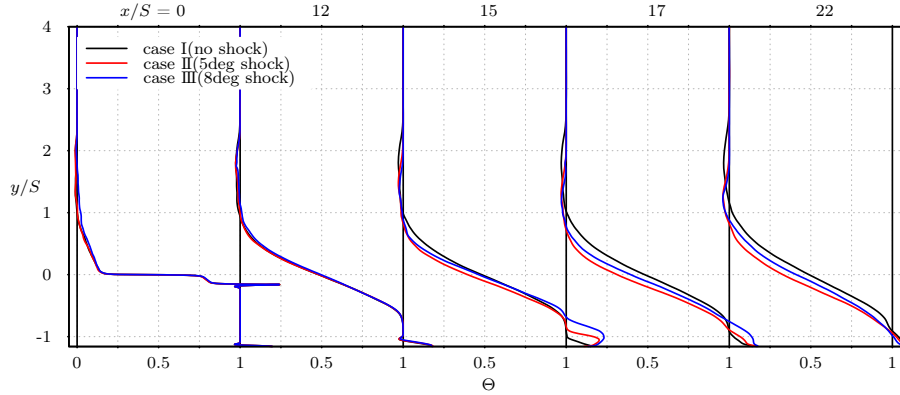


Figure 14: Dimensionless fluid temperature profiles Θ at several downstream positions

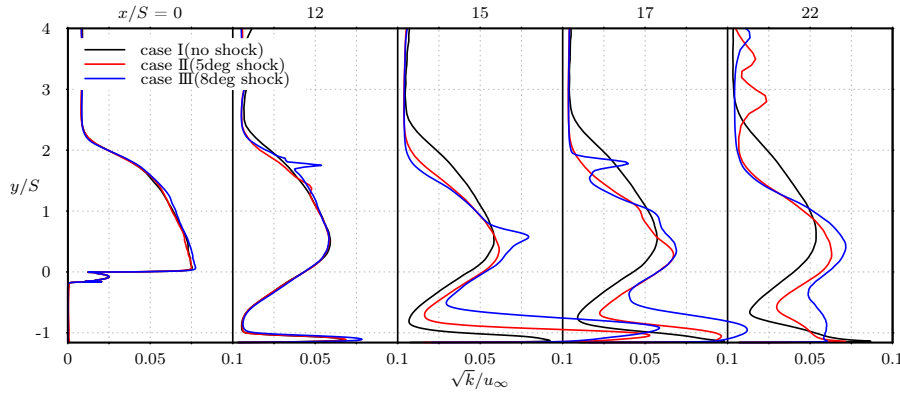


Figure 15: Turbulent kinetic energy profiles.

case III is larger than that of case II due to the stronger shock. Hence, the shock wave interaction upon the potential-core region leads to the transition to turbulence of the laminar slot boundary layer. The results show that the higher values for cases II and III compared to case I downstream of the shock impingement position lead to a steeper slope in the cooling effectiveness in Fig. 13.

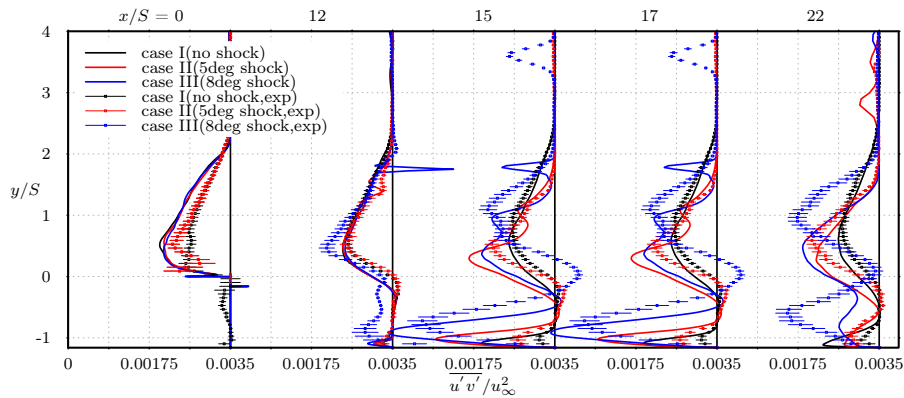


Figure 16: Reynolds shear stress

The experimental results obtained by Particle Image Velocimetry (PIV) measurements, are shown as dots with error bar in Fig. 16. A good agreement of the results is visible for case I. However, after $x/S = 15$ the amplitude of the fluctuations near the wall is smaller in the experiment than in the LES results. Downstream of the streamwise position $x/S = 15$ of case II the experimental values are larger compared to the LES results in the shear stress region, while on the other hand near the wall, the absolute value is smaller than in the LES results. The minimum peak of case III near the wall occurs at $y/S = 0.2$ in the experiment which is higher than in the LES results. For cases II and III after the shock reflection the Reynolds shear stress is shifted upwards compared to the LES results due to the slightly different position of the reflection, i.e., the experimental location is more upstream than that of the LES results. For case III, the Reynolds shear stresses around the shock impingement position near the wall are different than that of the LES results. This is caused by a different shock wave angle, which is approximately 2° larger in the experimental setup than in the LES. The larger shock angle produces a larger separation bubble, thus, the area of transition of momentum at case III is larger than that of case II. Overall, the results of the experiment show quantitatively and due to the different shock angle qualitatively good agreement with the LES results.

5 Conclusion

Large-eddy simulation of shock-cooling-film interactions were performed and validated by the experimental data. A laminar cooling flow at Mach number $Ma_i = 1.8$ was injected into a supersonic turbulent boundary layer at Mach number $Ma_\infty = 2.44$. The shock waves impinge upon the potential-core (cases II and III). At the shock-wave impingement position within the potential-core region for both cases the transition of the laminar slot boundary layer to turbulence occurs downstream of the separation bubble. The stronger shock induces a larger separation bubble than the weak shock wave. The increased turbulence levels in the shear- and mixing layer located between the cooling flow and the freestream lead to a maximum decrease of cooling effectiveness compared to a zero-pressure gradient configuration (case I) of 4.6% at case II. The stronger 8° shock wave at the same impingement position leads to a maximum decrease of the cooling effectiveness of 13.4%. At increasing shock strength at the further downstream impingement position (case III), the cooling effectiveness decreases even more rapidly, i.e., the streamwise cooling effectiveness shows a steeper gradient.

References

- [1] K. A. Juhany, M. L. Hunt, and J. M. Sivo. Influence of injectant mach number and temperature on supersonic film cooling. *Journal of Thermophysics and Heat Transfer*, 8(1):59–67, 1994.
- [2] M. Konopka, M. Meinke, and W. Schröder. Large-eddy simulation of high mach number film cooling with shock-wave interaction. *Progress in Flight Physics*, 5:309–326, 2013.
- [3] M. Konopka, M. Meinke, and W. Schröder. Large-eddy simulation of shock-cooling-film interaction at helium and hydrogen injection. *Phys. Fluids*, 25(10):106101, 2013.
- [4] R. A. Seban and L. H. Back. Velocity and temperature profiles in turbulent boundary layers with tangential injection. *Journal of Heat Transfer*, 84(1):45–54, 02 1962.
- [5] E. Alzner and V. Zakky. Turbulent boundary-layer shock interaction with and without injection. *AIAA Journal*, 9(9):1769–1776, 1971.
- [6] T. Kanda, F. Ono, M. Takahashi, T. Saito, and Y. Wakamatsu. Experimental studies of supersonic film cooling with shock wave interaction. *AIAA Journal*, 34(2):265–271, 1996.
- [7] T. Kanda and F. Ono. Experimental studies of supersonic film cooling with shock wave interaction (ii). *Journal of Thermophysics and Heat Transfer*, 11(4):590–592, 1997.
- [8] P. Marquardt, F. Michaux, and M. Klaas. PIV measurements of supersonic slot-film cooling with shock/cooling-film interaction. In *18th International Symposium on the Application of Laser and Imaging Techniques to Fluid Mechanics, LISBON*, 2016.
- [9] P. Marquardt, M. Klaas, and W. Schröder. PIV measurements of shock/cooling-film interaction at varying shock impingement position. In Andreas Dillmann, Gerd Heller, Ewald Krämer, Claus Wagner, Stephan Bansmer, Rolf Radespiel, and Richard Semaan, editors, *New Results in Numerical and Experimental Fluid Mechanics XI: Contributions to the 20th STAB/DGLR Symposium Braunschweig, Germany, 2016*, pages 129–139, Cham, 2018. Springer International Publishing.

- [10] S. Pirozzoli and M. Bernardini. Turbulence in supersonic boundary layers at moderate Reynolds number. *Journal of Fluid Mechanics*, 688:120–168, 2011.
- [11] S. Pirozzoli and M. Bernardini. Probing high-reynolds-number effects in numerical boundary layers. *Physics of Fluids*, 25(2):021704, 2013.
- [12] M. Bernardini and S. Pirozzoli. Inner/outer layer interactions in turbulent boundary layers: A refined measure for the large-scale amplitude modulation mechanism. *Physics of Fluids*, 23(6):061701, 2011.
- [13] B. Aupoix, A. Mignosi, S. Viala, F. Bouvier, and R. Gaillard. Experimental and numerical study of supersonic film cooling. *AIAA Journal*, 36(6):915–923, 1998.
- [14] M.-S. Liou and C.J. Steffen. A new flux splitting scheme. *Journal of Computational Physics*, 107(1):23 – 39, 1993.
- [15] F. G. Schmitt. About Boussinesq’s turbulent viscosity hypothesis: historical remarks and a direct evaluation of its validity. *Comptes Rendus Mécanique*, 335(9):617 – 627, 2007. Joseph Boussinesq, a Scientist of bygone days and present times.
- [16] B. Roidl, M. Meinke, and W. Schröder. A reformulated synthetic turbulence generation method for a zonal rans-les method and its application to zero-pressure gradient boundary layers. *International Journal of Heat and Fluid Flow*, 44:28 – 40, 2013.
- [17] P. G. Huang and G. N. Coleman. Van Driest transformation and compressible wall-bounded flows. *AIAA Journal*, 32(10):2110–2113, 1994.